ACS Energy LETTERS

http://pubs.acs.org/journal/aelccp

Local Background Hole Density Drives Nonradiative Recombination in Tin Halide Perovskites

Robert J. E. Westbrook, Margherita Taddei, Rajiv Giridharagopal, Meihuizi Jiang, Shaun M. Gallagher, Kathryn N. Guye, Aaron I. Warga, Saif A. Haque, and David S. Ginger*

Cite This: *ACS Energy Lett.* 2024, 9, 732−739

Read Online

ACCESS | Metrics & More | Article Recommendations | Supporting Information

ABSTRACT: We use multimodal microscopy to study carrier recombination in semiconducting tin halide perovskite films based on $\mathrm{PEA_{0.2}FA_{0.8}SnI_3}$ (PEA = phenethylammonium; FA = formamidinium). We use the observation of pseudo-first-order photoluminescence (PL) decay kinetics to establish a method for quantifying the hole dopant level and nonradiative recombination rate constant. We find that untreated $\mathrm{PEA_{0.2}FA_{0.8}SnI_3}$ films exhibit large hole doping concentrations of $p_0 \approx 10^{19}$ cm^{-3}, which is reduced to $p_0 \approx 10^{16}$ cm^{-3} after $\mathrm{SnF_2}$ treatment. While it is well-known that the radiative recombination rates are increased with p_0, we reveal that the nonradiative rate is also increased. We find that *p*-type regions in untreated $\mathrm{PEA_{0.2}FA_{0.8}SnI_3}$ films are centers for nonradiative recombination, which are diminished in films with $p_0 \approx 10^{16}$ cm^{-3}. We discover significant PL heterogeneity even in $\mathrm{PEA_{0.2}FA_{0.8}SnI_3}$ films with moderate dopant levels, suggesting that new strategies to eliminate deleterious defects in $\mathrm{PEA_{0.2}FA_{0.8}SnI_3}$ must be developed.

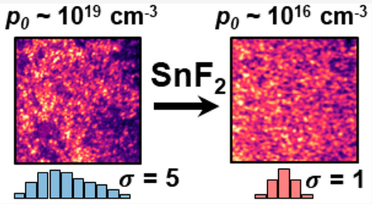

Tin halide perovskites, with the general formula $\mathrm{ABX_3}$ [A = Formamidinium (FA), B = Sn, X = Br, I], offer a narrower bandgap (~1.3 eV) than their lead counterparts, making them suitable candidates for the light-absorbing semiconductor in single-junction photovoltaic devices. Moreover, this attribute makes tin halide perovskites useful for all-perovskite tandems, with the best-performing cells incorporating a 50−50 Sn−Pb composition in the low bandgap component.[1−3] Nevertheless, record-breaking pure-Sn devices still exhibit severe losses in both the open-circuit voltage (V_{oc}) and short-circuit current (J_{sc}). These losses have kept power conversion efficiencies (PCEs) well below theoretical limits (cf. 14.6%, certified at a bandgap of 1.4 eV where the theoretical limit under AM1.5 illumination would be ~33%).[4]

Theoretical and experimental studies link the V_{oc} losses in $\mathrm{PEA_{0.2}FA_{0.8}SnI_3}$ to a complex chain of reactions starting with the formation of Sn vacancies ($\mathrm{V_{Sn}}$):[5,6]

$$\mathrm{Sn_{Sn}} \rightarrow \mathrm{Sn_{ex}} + \mathrm{V_{Sn}^{2-}} + 2\mathrm{h}^+ \qquad (1)$$

In eq 1, $\mathrm{Sn_{Sn}}$ is Sn(II) incorporated into the perovskite lattice at a Sn site, $\mathrm{Sn_{ex}}$ is metallic Sn(0) not embedded in the lattice, and $2\mathrm{h}^+$ represents the two excess holes generated to maintain charge neutrality.[7] Moreover, if a significant concentration of $\mathrm{Sn^{4+}}$ is present in the precursor solution, either due to $\mathrm{SnI_4}$ impurities in the $\mathrm{SnI_2}$ precursor[6] or direct oxidation of $\mathrm{SnI_2}$ in solution by dimethyl sulfoxide (DMSO),[8] $\mathrm{Sn^{4+}}$ can be reduced back to $\mathrm{Sn^{2+}}$ in the bulk, producing two holes as follows:[6,9,10]

$$\mathrm{Sn_{ex}^{4+}} \rightarrow \mathrm{Sn_{ex}^{2+}} + 2\mathrm{h}^+ \qquad (2)$$

Otherwise, $\mathrm{Sn^{4+}}$ is stabilized at the Sn perovskite surface as a deep electron trap.[11] Nonradiative V_{oc} loss is directly linked to decreases in the photoluminescence quantum yield (PLQY) and thus the prevalence of nonradiative recombination.[11] Additionally, reports have shown that high hole doping levels can lead to fast recombination and blue-shifted absorbance via the Burstein−Moss effect, both of which work to reduce the J_{sc}.[12−16]

Strategies for improving the PCE of perovskite solar cells based on $\mathrm{PEA_{0.2}FA_{0.8}SnI_3}$ have focused on mitigating the formation of V_{sn}, usually by incorporating excess $\mathrm{Sn^{2+}}$ ions in the form of $\mathrm{SnF_2}$ and imposing a higher V_{sn} formation energy with 2D layer functionalization.[17−21] Given that the V_{OC} is directly linked to the PLQY, ensemble steady-state and transient PL spectroscopy techniques are useful tools to assess performance.[15,22−25] Aside from ensemble photoluminescence (PL) behavior, microscale photoluminescence heterogeneity has provided important insights in both traditional III−IV

Received: December 13, 2023
Revised: January 23, 2024
Accepted: January 24, 2024
Published: January 31, 2024

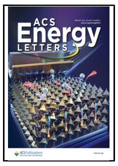

ACS Publications

https://doi.org/10.1021/acsenergylett.3c02701

semiconductor photovoltaics and Pb perovskites[11,26−34] but remains less used for Sn perovskites.

Here, we use a combination of spectroscopy, microscopy, and device characterization to assess heterogeneity in $PEA_{0.2}FA_{0.8}SnI_3$ while modulating the hole doping level, p_0 with SnF_2 treatment. We developed an all-optical method to extract p_0 from the PLQY and time-resolved PL lifetime. We show that untreated $PEA_{0.2}FA_{0.8}SnI_3$ has a large hole dopant level ($p_0 \approx 10^{19}$ cm^{-3}) and exhibits significant microscale variations in both the bandgap and PL intensity. Treatment with 10 mol % SnF_2 both lowers the hole dopant level ($p_0 \approx 10^{16}$ cm^{-3}) and reduces the PL heterogeneity. Correlated conductive atomic force microcopy (c-AFM) and photoluminescence spectroscopy reveal that the nonradiative recombination centers are mostly removed in $PEA_{0.2}FA_{0.8}SnI_3$ films with moderate dopant levels.

We studied $PEA_{0.2}FA_{0.8}SnI_3$ films prepared on glass substrates by spin-coating a stoichiometric mixture of tin iodide (SnI_2), formamidinium iodide (FAI), and phenethylammonium iodide (PEAI) in a mixture of dimethyl sulfoxide (DMSO) and *N*,*N*-dimethylformamide (DMF) following the method of Lanzetta et al. (more details in the Supporting Information).[6] In addition, we used a small amount of SnF_2 additive in the precursor solution to provide an excess of Sn^{2+} ions and limit V_{Sn} formation.[6] Furthermore, we encapsulated the films to eliminate the impact of atmospheric oxygen on their photophysical properties (Figure S1). We made photovoltaic cells under identical conditions and obtained power conversion efficiencies up to 8.26%, which is comparable to efficiencies in other reports using this architecture (Figure S2).[35,36] Notably, after addition of 10 mol % SnF_2 to the precursor solution, we observe a dramatic improvement in PCE from 2.72 ± 0.52% to 7.43 ± 0.50%, which we attribute to an improvement in both the open-circuit voltage (V_{OC}; 0.495 ± 0.01 V to 0.555 ± 0.01 V) and short-circuit current (J_{SC}; 8.16 ± 1.54 mA cm^{-2} to 20.45 ± 0.96 mA cm^{-2}). We provide further device characterization statistics in Figure S3.

Previous studies have used steady-state PL spectroscopy to deduce qualitative information about p_0 and nonradiative decay rates in Sn perovskites such as $PEA_{0.2}FA_{0.8}SnI_3$.[15,22,25] Figure 1a shows the ensemble steady-state photoluminescence characteristics of an untreated $PEA_{0.2}FA_{0.8}SnI_3$ film and one that was made after the addition of 5% SnF_2 to the precursor solution. These treatments increase (redshift) the PL peak wavelength and narrow the PL spectrum. The decrease in peak PL wavelength is consistent with the expected decrease of the Burstein−Moss shift associated with reduced band-filling from excess *p*-type carriers as the doping level decreases.[15,16] The narrowing of the PL spectrum may also be associated with a decrease in doping-related heterogeneity.[22] As such, both the full width at half-maximum (fwhm) and peak position of PL spectra provide a method for *qualitatively* assessing the hole doping level.

We next combine time-resolved PL, measured with time-correlated single-photon counting (TCSPC), and PLQY to extract *quantitative* information about p_0 and the nonradiative recombination rate constant (k_{nr}). Using SnF_2 additive treatment,[6] we produced a series of $PEA_{0.2}FA_{0.8}SnI_3$ films with different PL lifetimes and thus presumably different p_0 and k_{nr}. We show the TRPL and PLQY data for an example $PEA_{0.2}FA_{0.8}SnI_3$ film treated with 5% SnF_2 additive in Figure 1b,c (this data for the other $PEA_{0.2}FA_{0.8}SnI_3$ films is provided in Figures S4−S9 and Table S1).

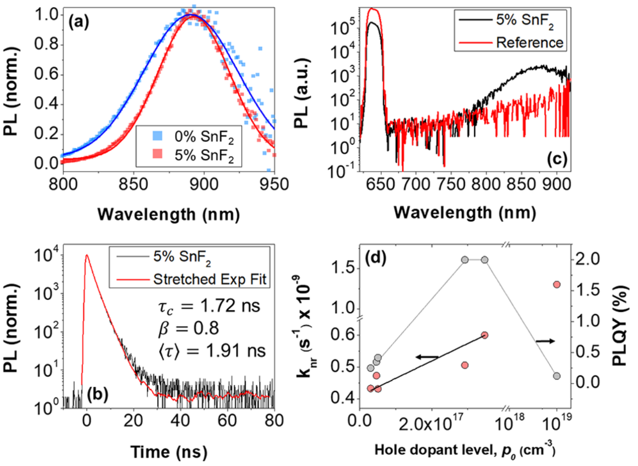

Figure 1. (a) Steady-state photoluminescence of $PEA_{0.2}FA_{0.8}SnI_3$ films on glass substrates with (red) and without (blue) 5% SnF_2. (b) Time-correlated single-photon counting (TCSPC) decay, and corresponding stretched exponential fit, of a $PEA_{0.2}FA_{0.8}SnI_3$ film made with 5% SnF_2 additive. (c) PL spectra of $PEA_{0.2}FA_{0.8}SnI_3$ treated with 5% SnF_2 additive (black) and glass reference (red) used to find the PLQY. (d) Plot of the nonradiative rate constant, k_{nr} (red circles), and PLQY (gray circles), as a function of the hole dopant level, p_0 for the $PEA_{0.2}FA_{0.8}SnI_3$ films studied herein. The value of k_{nr} for the $p_0 \approx 10^{19}$ cm^{-3} sample is a minimum based on the instrumental response of the TCSPC set up (0.5 ns). The linearity of the k_{nr} plot in the 10^{16}−10^{17} cm^{-3} range suggests that the nonradiative recombination stems from first-order processes, such as charge trapping.

In the limit of low excitation fluence, the photoluminescence decay associated with electron−hole recombination in a doped semiconductor is characterized by first-order kinetics:[25,37]

$$PL(t) \propto e^{-(k_{nr}+k_{bi}p_0)t} \tag{3}$$

Here, k_{nr} is the rate constant for nonradiative decay of minority (*n*-type) carriers and k_{bi} is the bimolecular radiative rate constant; we fit the decay in Figure 1b to a stretched exponential[31,38,39]

$$PL(t) \propto e^{[-(k_{nr}+k_{bi}p_0)t]^{\beta}} \tag{4}$$

where β is the stretching parameter associated with the stretched exponential. The stretched exponential form of the ensemble decay in this case has a physical origin in the summing of single exponential decays of the form given in eq 3, where the β value carries information about how broad the lifetime distribution is. $\beta = 1$ recovers a homogeneous single exponential, and lower values of β arise from more distributed kinetics.[31,39] Equation 5 gives the average lifetime from the stretched exponential, $\langle\tau\rangle$[38−40]

$$\langle\tau\rangle = \frac{\tau_c}{\beta}\Gamma\left(\frac{1}{\beta}\right) \tag{5}$$

where Γ is the gamma function and τ_c is the characteristic lifetime of the stretched exponential. The $PEA_{0.2}FA_{0.8}SnI_3$ sample prepared with 5% SnF_2 additive decays with a $\langle\tau\rangle$ of 1.9 ns. This is at least four times slower than the decay of the untreated $PEA_{0.2}FA_{0.8}SnI_3$ sample, which is limited by the instrumental response ($\langle\tau\rangle < 0.5$ ns). However, with TCSPC alone, it is impossible to say whether this decrease in lifetime is due to an increase in k_{nr}, an increase in p_0, or both.

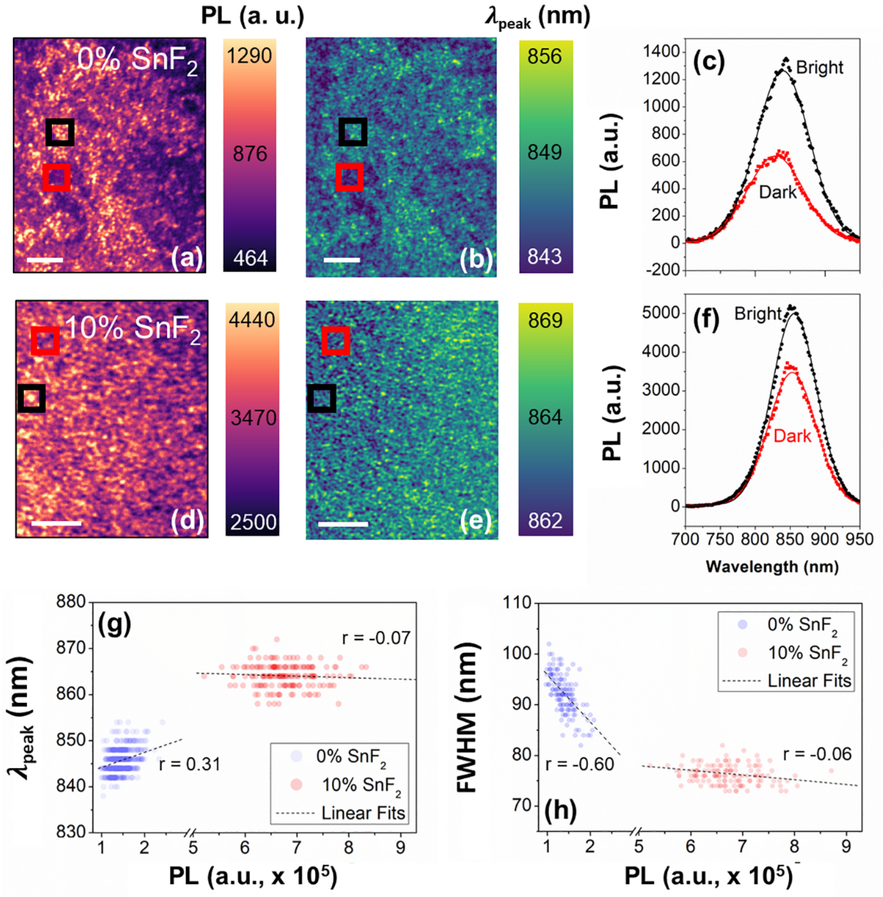

Figure 2. (a) Intensity at 848 nm and (b) peak wavelength maps of an untreated $PEA_{0.2}FA_{0.8}SnI_3$ film. (c) Local PL spectra taken in the labeled bright (black) and dark (red) regions of the hyperspectral images in panels a and b. The PL spectra are fitted to a Gaussian distribution. (d) Intensity at 864 nm and (e) peak wavelength maps of a $PEA_{0.2}FA_{0.8}SnI_3$ film after 10% SnF_2 treatment. (f) Local PL spectra taken in the labeled bright (black) and dark (red) regions of the hyperspectral images in panels d and e. The PL spectra are fitted to a Gaussian distribution. Films were excited with a 532 nm laser at a power of 10 W cm^{-2}. The scalebars in all images are 10 μm. (g) Correlation between peak emission wavelength (λ_{peak}) and emission intensity for each pixel in the untreated (a and b) and treated (d and e) images. (h) Correlation between fwhm and integrated intensity at each pixel of the untreated (a and b) and treated (d and e) images. A regular skipping filter of 500 was applied to the data to reduce the number of data points visible in the plots.

We have previously found that the $\langle\tau\rangle$ calculated from stretched exponential decays is consistent with the PLQY across a range of systems.[39,40] In p-type $PEA_{0.2}FA_{0.8}SnI_3$, where the PLQY and $\langle\tau\rangle$ both depend on p_0, this relationship becomes

$$\mathrm{PLQY} = k_{bi}p_0\langle\tau\rangle = \frac{k_{bi}p_0}{k_{bi}p_0 + k_{nr}} \tag{6}$$

Figure 1c shows the photoluminescence spectrum of the $PEA_{0.2}FA_{0.8}SnI_3$ sample treated with 5% SnF_2 additive and a glass reference, captured after exciting the samples in an integrating sphere. We used these spectra to extract the PLQY, which was 2.0%. Therefore, by combining PLQY and TRPL measurements in the same fluence limit and using our calculated value for k_{bi} (~3.6×10^{-11} cm^3 s^{-1}, see Figures S10−S12), we can extract p_0 and k_{nr}. Importantly, in the fluence range that we adopt (10^{13}−10^{15} cm^{-3}), neither the PL lifetime (eqs 3−5) nor the PLQY (eq 6) are dependent upon the carrier density (n), meaning that the requirement to match carrier densities in PLQY and TRPL measurements is relaxed (Figures S13 and S14). We calculate the example $PEA_{0.2}FA_{0.8}SnI_3$ film to have a p_0 and k_{nr} of 2.9×10^{17} cm^{-3} and 5.1×10^{8} s^{-1}, respectively. We note that the upper estimation limit of this technique is limited, given that we cannot resolve recombination rates faster than ~2×10^{9} s^{-1} with our TCSPC system. Therefore, to estimate p_0 in these cases, we consider the bandgap shift associated with the Burstein−Moss band-filling effect and use the analysis of Milot et al. to roughly estimate p_0 (Figure S15).[25] Using this combined methodology, we confirm that our series of $PEA_{0.2}FA_{0.8}SnI_3$ films has p_0 ranging from 10^{19} down to 10^{16} cm^{-3}, spanning most of the p_0 values reported in the literature (Table S1).[25,41−44]

Figure 1d shows our measured PLQY and analysis of k_{nr} and p_0 for all of the $PEA_{0.2}FA_{0.8}SnI_3$ films studied here. The trend in PLQY can be split into two parts: (i) PLQY increasing with p_0 ($p_0 < 4 \times 10^{17}$ cm^{-3}), and (ii) PLQY decreasing with p_0 ($p_0 > 4 \times 10^{17}$ cm^{-3}). On the other hand, k_{nr} increases steadily with p_0 throughout the entire range, regardless of whether the PLQY is increasing or decreasing. Moreover, the values for k_{nr}, ranging from 4.3×10^{8} to above 1.3×10^{9} s^{-1}, remain larger than the corresponding pseudo-first-order radiative recombination rate constants ($k_{bi}p_0$), which range between 1.1×10^{6} and 3.6×10^{8} s^{-1}, consistent with the relatively low PLQY of these samples.

An important result from the analysis presented so far is that, in addition to having faster radiative decay of minority carriers due to the increase in the pseudo-first-order rate constant ($k_{bi}p_0$), more heavily p-doped films also show higher rates of *nonradiative* recombination. We hypothesize that the increase in nonradiative decay rate with increasing p_0 could arise from two different factors: (i) a direct relationship between the concentration of acceptor sites and trap-states, or (ii) two hole−one electron Auger−Meitner recombination events associated with the very high (up to 10^{19} cm^{-3}) densities of holes in these regions.[9] To test the second hypothesis, we consider the rate equation for Auger−Meitner recombination in a p-doped semiconductor where one electron (bulk density, n) recombines with two holes (bulk density, $p + p_0$):

$$\frac{-\mathrm{d}n}{\mathrm{d}t} = k_{\mathrm{Aug}}n(p + p_0)(p + p_0) \tag{7}$$

where k_{Aug} is the rate constant for Auger−Meitner recombination. This equation simplifies at the low fluences ($n, p \ll p_0$) studied here to a quadratic relationship:

$$\frac{-\mathrm{d}n}{\mathrm{d}t} = k_{\mathrm{Aug}}np_0^{\ 2} \tag{8}$$

On the other hand, if nonradiative recombination is governed by trap-mediated recombination, we would expect the following equation to govern the rate:

$$\frac{-\mathrm{d}n}{\mathrm{d}t} = k_{\mathrm{t}}n \tag{9}$$

where k_t is the rate constant for charge trapping. Therefore, we interpret the linear relationship between k_{nr} and p_0 observed in the $10^{16} < p_0 < 4 \times 10^{17}$ cm^{-3} region (Figure 1d) as evidence that the dominant recombination process is trap-mediated recombination. This can be rationalized in terms of the $PEA_{0.2}FA_{0.8}SnI_3$ materials chemistry (eqs 1 and 2), where high concentrations of Sn^{4+} are expected to lead to both a high p_0 and promote the formation of deep electron traps (increasing k_t).[5,10] We note that Auger−Meitner recombination events may provide an additional contribution to the higher nonradiative rate in heavily doped ($p_0 > 4 \times 10^{17}$ cm^{-3}) $PEA_{0.2}FA_{0.8}SnI_3$.[9]

We conducted hyperspectral PL microscopy on $PEA_{0.2}FA_{0.8}SnI_3$ samples with different dopant levels to better understand the origins of PL heterogeneity. The hyperspectral PL technique enables simultaneous characterization of spatial and spectral heterogeneity in photoluminescence intensity with high resolution.[45,46] We provide details of our measurements in the Supporting Information.

Figure 2a,b shows PL intensity and peak wavelength maps for $PEA_{0.2}FA_{0.8}SnI_3$ with $p_0 \approx 10^{19}$ cm^{-3}. Combined, these images show that untreated $PEA_{0.2}FA_{0.8}SnI_3$ is highly heterogeneous, characterized by microscale regions of red-shifted, high-intensity and blue-shifted, low-intensity PL. Figure 2c displays point spectra taken in dark (red box) and bright (black box) regions of the film. The peaks associated with the bright and dark regions have maxima at 840 and 830 nm, respectively. If we assume that local changes in energy are determined by p-type doping, the shift in the peak emission wavelength suggests that the brighter regions are 16 meV lower in energy than the darker regions. These data agree with our *ensemble* measurements above, where we find that very high dopant densities lead to lower PLQY. Here, we see that microscale regions of very high dopant density (as signified by local PL blue-shift) also have a lower PLQY. Figure 2d,e shows the PL intensity and peak wavelength maps for $PEA_{0.2}FA_{0.8}SnI_3$ with $p_0 \approx 10^{16}$ cm^{-3}. These images show that $PEA_{0.2}FA_{0.8}SnI_3$ is much more homogeneous after 10% SnF_2 treatment. Figure 2f presents point spectra taken at representative dark (red box) and bright (black box) regions of the film. The peaks associated with the bright and dark regions have their maxima at 856 and 852 nm, which represents a smaller energetic shift (~7 meV) as compared to the $p_0 \approx 10^{19}$ cm^{-3} film.

In Figure 2g,h we correlate qualitative metrics for the local p_0, namely, the PL peak wavelength (Figure 2g) and the PL fwhm (Figure 2h), to the PL intensity at each pixel of the hyperspectral images for the two film types. Figure 2g shows that for $PEA_{0.2}FA_{0.8}SnI_3$ with $p_0 \approx 10^{19}$ cm^{-3}, regions with longer PL peak wavelengths tend to have a higher PL intensity (moderate positive correlation, $r = 0.31$). This correlation becomes negligible ($r < 0.1$) in the $PEA_{0.2}FA_{0.8}SnI_3$ film with $p_0 \approx 10^{16}$ cm^{-3}. Similarly, Figure 2h shows that regions with narrower fwhm tend to have higher PL intensities (strong negative correlation, $r = -0.60$). This correlation becomes negligible ($|r| < 0.1$) in $PEA_{0.2}FA_{0.8}SnI_3$ with $p_0 \approx 10^{16}$ cm^{-3}. These correlations are strong indicators that the more heavily doped regions in the $p_0 \approx 10^{19}$ cm^{-3} film undergo more nonradiative recombination than the more weakly doped regions.

The correlation between local nonradiative rates and p_0 in $PEA_{0.2}FA_{0.8}SnI_3$ films with very high dopant levels can be rationalized in terms of the $PEA_{0.2}FA_{0.8}SnI_3$ material chemistry (eqs 1 and 2), where high concentrations of Sn^{4+} are expected to lead to both a high p_0 and promote the formation of deep electron traps.[5,10] These two factors generate the perfect storm for nonradiative recombination, given that trapped electrons are more quickly annihilated by valence band holes in a strongly p-doped system. This should lead to increased nonradiative recombination and loss of device J_{SC} and V_{OC}. We note this model contrasts with the one developed by Frohna et al. for p-type Pb-based perovskites, where it was found that the p-type regions had a higher PLQY and thus conduct photocarriers away from potential trap sites in the lower conductivity, low-PLQY regions.[30] We note that Auger−Meitner recombination events may provide an additional contribution to the higher nonradiative rate in heavily doped regions of untreated $PEA_{0.2}FA_{0.8}SnI_3$ films, where the dopant level is very high ($p_0 \approx 10^{19}$ cm^{-3}).[9]

The plot of PL fwhm against the PL intensity for $PEA_{0.2}FA_{0.8}SnI_3$ with $p_0 \approx 10^{16}$ cm^{-3} reveals no obvious correlation. Therefore, we devised a more sensitive experiment to clarify the relationship between the local p_0 and PL intensity. Specifically, we correlated hyperspectral PL with conducting atomic force microscopy (c-AFM) carried out in the dark. Because we performed c-AFM in the dark, we attribute the variations in local current to variations in local p-doping. We provide representative AFM topography images of $PEA_{0.2}FA_{0.8}SnI_3$ films with $p_0 \approx 10^{19}$ cm^{-3} and $p_0 \approx 10^{16}$ cm^{-3} in Figure S16. We compare dark $J-V$ scans of $PEA_{0.2}FA_{0.8}SnI_3$ with $p_0 \approx 10^{19}$ cm^{-3} and $p_0 \approx 10^{16}$ cm^{-3} in Figure S17.

In Figure 3a,b, we present a hyperspectral PL image and c-AFM image of the same region of the same $PEA_{0.2}FA_{0.8}SnI_3$ film treated with 10% SnF_2 additive. In Figure 3c, we plot the PL intensity against the dark current for each pixel of the PL image. We find a weak ($r \approx 0.18$) negative correlation between the magnitude of the current and the PL intensity at each pixel

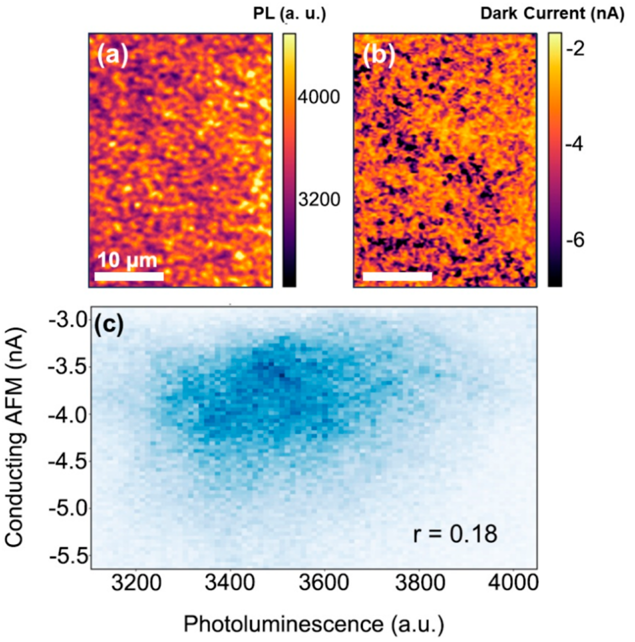

Figure 3. Correlation of local dark current and photoluminescence intensity in a $PEA_{0.2}FA_{0.8}SnI_3$ film treated with 10% SnF_2 additive. (a) Photoluminescence (PL) intensity map obtained from hyperspectral microscopy for a $PEA_{0.2}FA_{0.8}SnI_3$ film treated with 10% SnF_2 additive, measured at 10 W cm^{-2}. (b) Conducting atomic force microscopy (c-AFM) image of the same area of the film (sample bias = −0.2 V). The scalebars represent 10 μm. (c) Correlation plot of the current from c-AFM and photoluminescence intensity from hyperspectral PL images.

of the image. These data show that SnF_2 treatment is an effective measure for minimizing the *p*-type nonradiative recombination centers that we observe in untreated $PEA_{0.2}FA_{0.8}SnI_3$.

The weak ($r \approx 0.18$) but significant negative correlation between the magnitude of the current and the PL intensity bears some discussion. So far, we have experimentally demonstrated the theoretically predicted[10] link between the formation of hole dopants and defect states that lead to nonradiative recombination. One interpretation of the data in Figure 3c would be that higher local hole dopant levels lead to more nonradiative recombination, consistent with our finding that k_{nr} increases with p_0. This would suggest that even in $PEA_{0.2}FA_{0.8}SnI_3$ films with state-of-the-art dopant management strategies, there is still a link between local dopant level and the formation of defects that act as nonradiative recombination centers. An alternative explanation for the observed correlation is that the regions of lower current are due to a higher local concentration of insulating SnF_2. However, we note that SnF_2 is known to form submicrometer scale crystallites on $PEA_{0.2}FA_{0.8}SnI_3$ surfaces,[47] which do not match with the length scale of current variations in Figure 3b and which were not observed in AFM topography (Figure S16).

Figure 4a,b displays histogram data of the peak PL wavelength across all pixels of the hyperspectral PL images in two limiting cases: (a) $PEA_{0.2}FA_{0.8}SnI_3$ with 10% SnF_2 additive (p_0 = 5.1 × 10^{16} cm^{-3}) and (b) $PEA_{0.2}FA_{0.8}SnI_3$ with no treatment ($p_0 \approx 10^{19}$ cm^{-3}). These data clearly show a trend of decreasing bandgap with decreasing p_0, which is in line with previous reports of the Burstein−Moss effect in highly doped $ASnI_3$ derivatives.[22,25] Figure S15 shows that the shift in E_g is minimal below a carrier density of 1 × 10^{17} cm^{-3}. Importantly, the narrowing of the peak PL wavelength distribution as the dopant level is reduced (Figure 4b to 4a) suggests that the SnF_2 additive treatment reduces the photoluminescence heterogeneity.

We use the standard deviation of the peak emission wavelength, σ_λ, and emission intensity (normalized to the mean), σ_{PL}/μ_{PL}, as metrics for quantifying PL heterogeneity. Given the significant reduction of σ_λ (3.5×) and σ_{PL}/μ_{PL} (2×) that we observe when moving between $PEA_{0.2}FA_{0.8}SnI_3$ with $p_0 \approx 10^{19}$ cm^{-3} and $PEA_{0.2}FA_{0.8}SnI_3$ with $p_0 \approx 10^{16}$ cm^{-3}, we decided to measure these parameters for a wider range of samples with different p_0 (Figure 4c,d). We include the original

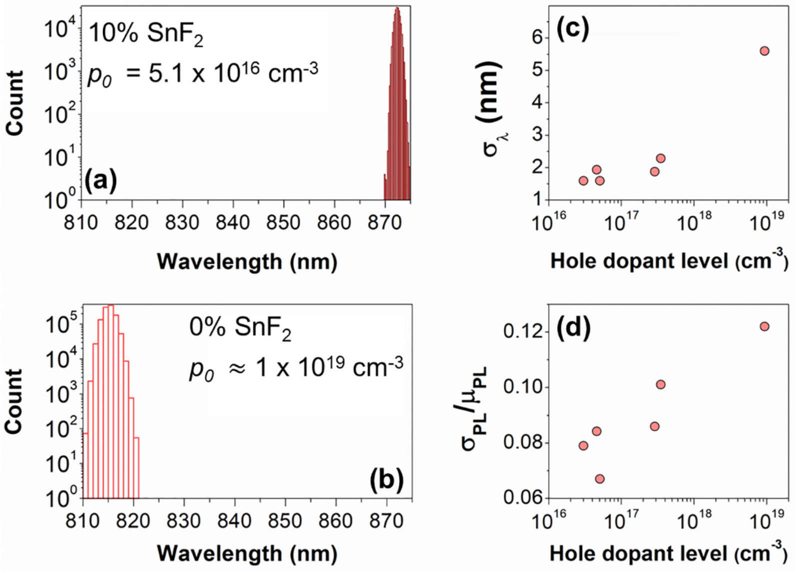

Figure 4. (a and b) Peak wavelength histograms of $PEA_{0.2}FA_{0.8}SnI_3$ with different hole doping levels, p_0 after (a) 10% SnF_2 additive treatment and (b) no treatment. (c and d) Standard deviation of (c) the peak wavelength, and (d) the PL intensity (normalized to the mean) as a function of p_0 for all $PEA_{0.2}FA_{0.8}SnI_3$ films in this study. The power used for these measurements was 4 W cm^{-2}.

hyperspectral PL images and associated histograms used for the analysis in Figures S18−S23. Figure 4c shows that the heterogeneity in peak PL wavelength is reduced by several times between 10^{19} and 10^{17} cm^{-3} before beginning to plateau toward 10^{16} cm^{-3}. On the other hand, Figure 4d reveals that the heterogeneity in the PL intensity (σ_{PL}/μ_{PL}) decreases monotonically between 10^{19} and 10^{16} cm^{-3} without reaching a plateau. This suggests that although SnF_2 treatment can reduce the microscale heterogeneity in PL intensity, additional gains could be achieved with a further reduction of p_0.

Overall, these data show that heterogeneity in both PLQY (as signified by σ_{PL}/μ_{PL}) and p_0 (as signified by σ_λ) are reduced with SnF_2 additive treatment. PL heterogeneity in perovskites overall is widely thought to stem from inhomogeneous crystal growth, leading to local variations in nonradiative recombination, for example due to microscale changes in composition, strain, and the aspect ratio of grains. These effects are exacerbated in $PEA_{0.2}FA_{0.8}SnI_3$ and other Sn-based halide perovskites, which undergo faster nucleation than Pb-based perovskites.[45] The addition of SnF_2 into the precursor solution and removal of Sn^{4+} impurities reduce these microscale variations, for example by limiting the formation of V_{Sn}, which would otherwise lead to the formation of trap states and excess holes. However, significant PL heterogeneity remains even in films that have undergone extensive Sn^{4+} management treatments. This would suggest that more work needs to be done to limit self-doping in state-of-the-art $PEA_{0.2}FA_{0.8}SnI_3$ films, perhaps by introducing complementary chemical strategies that target other defects. One such strategy would be finding complementary additive treatments that can effectively limit the formation of iodide interstitials from I_2, a process that introduces additional background holes to the $PEA_{0.2}FA_{0.8}SnI_3$ lattice.[7]

We have applied time-resolved photoluminescence and multimodal microscopy, including both hyperspectral photoluminescence microscopy and atomic force microscopy to $PEA_{0.2}FA_{0.8}SnI_3$ semiconductors prepared with different amounts of SnF_2 additive to study the effects of dopant levels and defect densities on carrier recombination kinetics. Our investigations reveal that untreated $PEA_{0.2}FA_{0.8}SnI_3$ is characterized by high levels of *p*-doping (~10^{19} cm^{-3}) and severe microscale heterogeneity in both the photoluminescence quantum yield (PLQY) and bandgap. Specifically, untreated $PEA_{0.2}FA_{0.8}SnI_3$ is permeated with poor-quality *p*-type channels that act as nonradiative recombination centers for photocarriers. Addition of SnF_2 to the precursor solution reduces the *p*-doping within the film by 1000× to around 10^{16} cm^{-3} and improves both the open-circuit voltage (V_{OC}) and short-circuit current (J_{SC}). These findings not only identify a key nonradiative recombination pathway in $PEA_{0.2}FA_{0.8}SnI_3$ but also reveal that further improvement in doping levels and microscale heterogeneity can pave the way for improved performance in $PEA_{0.2}FA_{0.8}SnI_3$ and related Sn perovskites.

ASSOCIATED CONTENT

Supporting Information

The Supporting Information is available free of charge at https://pubs.acs.org/doi/10.1021/acsenergylett.3c02701.

> Experimental methods, statistical data, photoluminescence quantum yield characterizations, and PLQY data (PDF)

AUTHOR INFORMATION

Corresponding Author

David S. Ginger − *Department of Chemistry, University of Washington, Seattle, Washington 98195, United States; Physical Sciences Division, Physical and Computational Sciences Directorate, Pacific Northwest National Laboratory, Richland, Washington 99352, United States;* orcid.org/0000-0002-9759-5447; Email: dginger@uw.edu

Authors

Robert J. E. Westbrook − *Department of Chemistry, University of Washington, Seattle, Washington 98195, United States*
Margherita Taddei − *Department of Chemistry, University of Washington, Seattle, Washington 98195, United States;* orcid.org/0000-0003-4122-8418
Rajiv Giridharagopal − *Department of Chemistry, University of Washington, Seattle, Washington 98195, United States;* orcid.org/0000-0001-6076-852X
Meihuizi Jiang − *Department of Chemistry and Centre for Processable Electronics, Molecular Sciences Research Hub, Imperial College London, London W12 0BZ, U.K.*
Shaun M. Gallagher − *Department of Chemistry, University of Washington, Seattle, Washington 98195, United States*
Kathryn N. Guye − *Department of Chemistry, University of Washington, Seattle, Washington 98195, United States;* orcid.org/0000-0003-1684-8084
Aaron I. Warga − *Department of Chemistry, University of Washington, Seattle, Washington 98195, United States;* orcid.org/0000-0001-6664-8465
Saif A. Haque − *Department of Chemistry and Centre for Processable Electronics, Molecular Sciences Research Hub, Imperial College London, London W12 0BZ, U.K.;* orcid.org/0000-0001-5483-3321

Complete contact information is available at: https://pubs.acs.org/10.1021/acsenergylett.3c02701

Notes

The authors declare no competing financial interest.

ACKNOWLEDGMENTS

The work at UW, including the contributions by R.W., M.T., and D.S.G, was primarily supported by the U.S. National Science Foundation through the UW Molecular Engineering Materials Center (MEM-C), a Materials Research Science and Engineering Center (DMR-1719797). The AFM imaging and analysis (R. G.) was supported by the Department of Energy Basic Energy Sciences, under Award DOE DE-SC0013957. D.S.G. and K.G. acknowledge support from the University of Washington Rabinovitch Endowment. S.A.H. acknowledges financial support from the Engineering and Physical Sciences Research Council (EPSRC Grant Number EP/R020574/1).

REFERENCES

(1) Eperon, G. E.; Leijtens, T.; Bush, K. A.; Prasanna, R.; Green, T.; Wang, J. T. W.; McMeekin, D. P.; Volonakis, G.; Milot, R. L.; May, R.; Palmstrom, A.; Slotcavage, D. J.; Belisle, R. A.; Patel, J. B.; Parrott, E. S.; Sutton, R. J.; Ma, W.; Moghadam, F.; Conings, B.; Babayigit, A.; Boyen, H. G.; Bent, S.; Giustino, F.; Herz, L. M.; Johnston, M. B.; McGehee, M. D.; Snaith, H. J. Perovskite-Perovskite Tandem Photovoltaics with Optimized Band Gaps. *Science* **2016**, *354*, 861−865.

(2) Lin, R.; Xu, J.; Wei, M.; Wang, Y.; Qin, Z.; Liu, Z.; Wu, J.; Xiao, K.; Chen, B.; Park, S. M.; Chen, G.; Atapattu, H. R.; Graham, K. R.; Xu, J.; Zhu, J.; Li, L.; Zhang, C.; Sargent, E. H.; Tan, H. All-Perovskite Tandem Solar Cells with Improved Grain Surface Passivation. *Nature* **2022**, *603* (7899), 73−78.

(3) Lin, R.; Xiao, K.; Qin, Z.; Han, Q.; Zhang, C.; Wei, M.; Saidaminov, M. I.; Gao, Y.; Xu, J.; Xiao, M.; Li, A.; Zhu, J.; Sargent, E. H.; Tan, H. Monolithic All-Perovskite Tandem Solar Cells with 24.8% Efficiency Exploiting Comproportionation to Suppress Sn(II) Oxidation in Precursor Ink. *Nat. Energy* **2019**, *4* (10), 864−873.

(4) Jiang, X.; Li, H.; Zhou, Q.; Wei, Q.; Wei, M.; Jiang, L.; Wang, Z.; Peng, Z.; Wang, F.; Zang, Z.; Xu, K.; Hou, Y.; Teale, S.; Zhou, W.; Si, R.; Gao, X.; Sargent, E. H.; Ning, Z. One-Step Synthesis of SnI2·(DMSO)X Adducts for High-Performance Tin Perovskite Solar Cells. *J. Am. Chem. Soc.* **2021**, *143* (29), 10970−10976.

(5) Meggiolaro, D.; Ricciarelli, D.; Alasmari, A. A.; Alasmary, F. A. S.; De Angelis, F. Tin versus Lead Redox Chemistry Modulates Charge Trapping and Self-Doping in Tin/Lead Iodide Perovskites. *J. Phys. Chem. Lett.* **2020**, *11* (9), 3546−3556.

(6) Lanzetta, L.; Webb, T.; Zibouche, N.; Liang, X.; Ding, D.; Min, G.; Westbrook, R. J. E.; Gaggio, B.; Macdonald, T. J.; Islam, M. S.; Haque, S. A. Degradation Mechanism of Hybrid Tin-Based Perovskite Solar Cells and the Critical Role of Tin (IV) Iodide. *Nat. Commun.* **2021**, *12* (1), 2853.

(7) Dey, K.; Roose, B.; Stranks, S. D. Optoelectronic Properties of Low-Bandgap Halide Perovskites for Solar Cell Applications. *Adv. Mater.* **2021**, *33* (40), 2102300.

(8) Pascual, J.; Nasti, G.; Aldamasy, M. H.; Smith, J. A.; Flatken, M.; Phung, N.; Di Girolamo, D.; Turren-Cruz, S. H.; Li, M.; Dallmann, A.; Avolio, R.; Abate, A. Origin of Sn(II) Oxidation in Tin Halide Perovskites. *Mater. Adv.* **2020**, *1* (5), 1066−1070.

(9) Treglia, A.; Ambrosio, F.; Martani, S.; Folpini, G.; Barker, A. J.; Albaqami, M. D.; De Angelis, F.; Poli, I.; Petrozza, A. Effect of Electronic Doping and Traps on Carrier Dynamics in Tin Halide Perovskites. *Mater. Horiz* **2022**, *9* (6), 1763−1773.

(10) Ricciarelli, D.; Meggiolaro, D.; Ambrosio, F.; De Angelis, F. Instability of Tin Iodide Perovskites: Bulk p-Doping versus Surface Tin Oxidation. *ACS Energy Lett.* **2020**, *5* (9), 2787−2795.

(11) Shi, Y.; Rojas-Gatjens, E.; Wang, J.; Pothoof, J.; Giridharagopal, R.; Ho, K.; Jiang, F.; Taddei, M.; Yang, Z.; Sanehira, E. M.; Irwin, M. D.; Silva-Acuña, C.; Ginger, D. S. (3-Aminopropyl)Trimethoxysilane Surface Passivation Improves Perovskite Solar Cell Performance by Reducing Surface Recombination Velocity. *ACS Energy Lett.* **2022**, *7* (11), 4081−4088.

(12) Herterich, J.; Baretzky, C.; Unmüssig, M.; Maheu, C.; Glissmann, N.; Gutekunst, J.; Loukeris, G.; Mayer, T.; Kohlstädt, M.; Hofmann, J. P.; Würfel, U. Toward Understanding the Short-Circuit Current Loss in Perovskite Solar Cells with 2D Passivation Layers. *Solar RRL* **2022**, *6* (7), 2200195.

(13) Shao, S.; Liu, J.; Portale, G.; Fang, H. H.; Blake, G. R.; ten Brink, G. H.; Koster, L. J. A.; Loi, M. A. Highly Reproducible Sn-Based Hybrid Perovskite Solar Cells with 9% Efficiency. *Adv. Energy Mater.* **2018**, *8* (4), 1702019.

(14) Thiesbrummel, J.; Le Corre, V. M.; Peña-Camargo, F.; Perdigón-Toro, L.; Lang, F.; Yang, F.; Grischek, M.; Gutierrez-Partida, E.; Warby, J.; Farrar, M. D.; Mahesh, S.; Caprioglio, P.; Albrecht, S.; Neher, D.; Snaith, H. J.; Stolterfoht, M. Universal Current Losses in Perovskite Solar Cells Due to Mobile Ions. *Adv. Energy Mater.* **2021**, *11* (34), 2101447.

(15) Savill, K. J.; Ulatowski, A. M.; Herz, L. M. Optoelectronic Properties of Tin-Lead Halide Perovskites. *ACS Energy Lett.* **2021**, *6* (7), 2413−2426.

(16) Jain, S. C.; McGregor, J. M.; Roulston, D. J. Band-Gap Narrowing in Novel III-V Semiconductors. *J. Appl. Phys.* **1990**, *68* (7), 3747−3749.

(17) Macdonald, T. J.; Lanzetta, L.; Liang, X.; Ding, D.; Haque, S. A. Engineering Stable Lead-free Tin Halide Perovskite Solar Cells: Lessons from Materials Chemistry. *Adv. Mater.* **2023**, *35*, 2206684.

(18) Lanzetta, L.; Webb, T.; Marin-Beloqui, J. M.; Macdonald, T. J.; Haque, S. A. Halide Chemistry in Tin Perovskite Optoelectronics: Bottlenecks and Opportunities. *Angewandte Chemie - International Edition* **2023**, *62*, No. e202213966.

(19) Nakamura, T.; Yakumaru, S.; Truong, M. A.; Kim, K.; Liu, J.; Hu, S.; Otsuka, K.; Hashimoto, R.; Murdey, R.; Sasamori, T.; Kim, H. Do; Ohkita, H.; Handa, T.; Kanemitsu, Y.; Wakamiya, A. Sn(IV)-Free Tin Perovskite Films Realized by in Situ Sn(0) Nanoparticle Treatment of the Precursor Solution. *Nat. Commun.* **2020**, *11* (1), 3008.

(20) Pitaro, M.; Tekelenburg, E. K.; Shao, S.; Loi, M. A. Tin Halide Perovskites: From Fundamental Properties to Solar Cells. *Adv. Mater.* **2022**, *34* (1), 2105844.

(21) Sanchez-Diaz, J.; Sánchez, R. S.; Masi, S.; Kreĉmarová, M.; Alvarez, A. O.; Barea, E. M.; Rodriguez-Romero, J.; Chirvony, V. S.; Sánchez-Royo, J. F.; Martinez-Pastor, J. P.; Mora-Seró, I. Tin Perovskite Solar Cells with > 1,300 h of Operational Stability in N2 through a Synergistic Chemical Engineering Approach. *Joule* **2022**, *6* (4), 861−883.

(22) Kahmann, S.; Shao, S.; Loi, M. A. Cooling, Scattering, and Recombination—The Role of the Material Quality for the Physics of Tin Halide Perovskites. *Adv. Funct Mater.* **2019**, *29* (35), 1902963.

(23) Westbrook, R. J. E.; Macdonald, T. J.; Xu, W.; Lanzetta, L.; Marin-Beloqui, J. M.; Clarke, T. M.; Haque, S. A. Lewis Base Passivation Mediates Charge Transfer at Perovskite Heterojunctions. *J. Am. Chem. Soc.* **2021**, *143* (31), 12230−12243.

(24) Westbrook, R. J. E.; Xu, W.; Liang, X.; Webb, T.; Clarke, T. M.; Haque, S. A. 2D Phase Purity Determines Charge-Transfer Yield at 3D/2D Lead Halide Perovskite Heterojunctions. *J. Phys. Chem. Lett.* **2021**, *12* (13), 3312−3320.

(25) Milot, R. L.; Klug, M. T.; Davies, C. L.; Wang, Z.; Kraus, H.; Snaith, H. J.; Johnston, M. B.; Herz, L. M. The Effects of Doping Density and Temperature on the Optoelectronic Properties of Formamidinium Tin Triiodide Thin Films. *Adv. Mater.* **2018**, *30* (44), 1804506.

(26) Doherty, T. A. S.; Winchester, A. J.; Macpherson, S.; Johnstone, D. N.; Pareek, V.; Tennyson, E. M.; Kosar, S.; Kosasih, F. U.; Anaya, M.; Abdi-Jalebi, M.; Andaji-Garmaroudi, Z.; Wong, E. L.; Madéo, J.; Chiang, Y. H.; Park, J. S.; Jung, Y. K.; Petoukhoff, C. E.; Divitini, G.; Man, M. K. L.; Ducati, C.; Walsh, A.; Midgley, P. A.; Dani, K. M.; Stranks, S. D. Performance-Limiting Nanoscale Trap Clusters at Grain Junctions in Halide Perovskites. *Nature* **2020**, *580* (7803), 360−366.

(27) Ni, Z.; Bao, C.; Liu, Y.; Jiang, Q.; Wu, W.-Q.; Chen, S.; Dai, X.; Chen, B.; Hartweg, B.; Yu, Z.; Holman, Z.; Huang, J. Resolving Spatial and Energetic Distributions of Trap States in Metal Halide Perovskite Solar Cells. *Science* **2020**, *367*, 1352−1358.

(28) Jariwala, S.; Sun, H.; Adhyaksa, G. W. P.; Lof, A.; Muscarella, L. A.; Ehrler, B.; Garnett, E. C.; Ginger, D. S. Local Crystal Misorientation Influences Non-Radiative Recombination in Halide Perovskites. *Joule* **2019**, *3* (12), 3048−3060.

(29) Correa-Baena, J.-P.; Luo, Y.; Brenner, T. M.; Snaider, J.; Sun, S.; Li, X.; Jensen, M. A.; Hartono, N. T. P.; Nienhaus, L.; Wieghold, S.; Poindexter, J. R.; Wang, S.; Meng, Y. S.; Wang, T.; Lai, B.; Holt, M. V.; Cai, Z.; Bawendi, M. G.; Huang, L.; Buonassisi, T.; Fenning, D. P. Homogenized Halides and Alkali Cation Segregation in Alloyed Organic-Inorganic Perovskites. *Science* **2019**, *363*, 627−631.

(30) Frohna, K.; Anaya, M.; Macpherson, S.; Sung, J.; Doherty, T. A. S.; Chiang, Y. H.; Winchester, A. J.; Orr, K. W. P.; Parker, J. E.; Quinn, P. D.; Dani, K. M.; Rao, A.; Stranks, S. D. Nanoscale Chemical Heterogeneity Dominates the Optoelectronic Response of Alloyed Perovskite Solar Cells. *Nat. Nanotechnol* **2022**, *17* (2), 190−196.

(31) DeQuilettes, D. W.; Vorpahl, S. M.; Stranks, S. D.; Nagaoka, H.; Eperon, G. E.; Ziffer, M. E.; Snaith, H. J.; Ginger, D. S. Impact of Microstructure on Local Carrier Lifetime in Perovskite Solar Cells. *Science* **2015**, *348* (6235), 683−686.

(32) Feldmann, S.; Macpherson, S.; Senanayak, S. P.; Abdi-Jalebi, M.; Rivett, J. P. H.; Nan, G.; Tainter, G. D.; Doherty, T. A. S.; Frohna, K.; Ringe, E.; Friend, R. H.; Sirringhaus, H.; Saliba, M.; Beljonne, D.; Stranks, S. D.; Deschler, F. Photodoping through Local Charge

Carrier Accumulation in Alloyed Hybrid Perovskites for Highly Efficient Luminescence. *Nat. Photonics* **2020**, *14* (2), 123−128.

(33) Pothoof, J.; Westbrook, R. J. E.; Giridharagopal, R.; Breshears, M. D.; Ginger, D. S. Surface Passivation Suppresses Local Ion Motion in Halide Perovskites. *J. Phys. Chem. Lett.* **2023**, *14*, 6092−6098.

(34) Chung, J.; Kim, S. W.; Li, Y.; Mariam, T.; Wang, X.; Rajakaruna, M.; Saeed, M. M.; Abudulimu, A.; Shin, S. S.; Guye, K. N.; Huang, Z.; Westbrook, R. J. E.; Miller, E.; Subedi, B.; Podraza, N. J.; Heben, M. J.; Ellingson, R. J.; Ginger, D. S.; Song, Z.; Yan, Y. Engineering Perovskite Precursor Inks for Scalable Production of High-Efficiency Perovskite Photovoltaic Modules. *Adv. Energy Mater.* **2023**, *13* (22), 2300595.

(35) Liao, M.; Yu, B.-B.; Jin, Z.; Chen, W.; Zhu, Y.; Zhang, X.; Yao, W.; Duan, T.; Djerdj, I.; He, Z. Efficient and Stable FASnI3 Perovskite Solar Cells with Effective Interface Modulation by Low-Dimensional Perovskite Layer. *ChemSusChem* **2019**, *12*, 5007−5014.

(36) Zeng, G.; Pu, D.; Huang, L.; Guan, H.; Zhou, S.; Zhou, J.; Shen, W.; Li, G.; Fang, G.; Ke, W. Enhancing the Performance of Tin-Based Perovskite Solar Cells through Solvent Purification of Tin Iodide. *J. Mater. Chem. A Mater.* **2023**, *11*, 11245.

(37) Nelson, J. *The Physics of Solar Cells*; Imperial College Press: London, 2003; pp 99−105.

(38) Dequilettes, D. W.; Koch, S.; Burke, S.; Paranji, R. K.; Shropshire, A. J.; Ziffer, M. E.; Ginger, D. S. Photoluminescence Lifetimes Exceeding 8 μs and Quantum Yields Exceeding 30% in Hybrid Perovskite Thin Films by Ligand Passivation. *ACS Energy Lett.* **2016**, *1* (2), 438−444.

(39) Munechika, K.; Chen, Y.; Tillack, A. F.; Kulkarni, A. P.; Plante, I. J. La; Munro, A. M.; Ginger, D. S. Spectral Control of Plasmonic Emission Enhancement from Quantum Dots near Single Silver Nanoprisms. *Nano Lett.* **2010**, *10* (7), 2598−2603.

(40) Wang, J.; Fu, W.; Jariwala, S.; Sinha, I.; Jen, A. K. Y.; Ginger, D. S. Reducing Surface Recombination Velocities at the Electrical Contacts Will Improve Perovskite Photovoltaics. *ACS Energy Lett.* **2019**, *4*, 222−227.

(41) Lee, S. J.; Shin, S. S.; Im, J.; Ahn, T. K.; Noh, J. H.; Jeon, N. J.; Seok, S., Il; Seo, J. Reducing Carrier Density in Formamidinium Tin Perovskites and Its Beneficial Effects on Stability and Efficiency of Perovskite Solar Cells. *ACS Energy Lett.* **2018**, *3* (1), 46−53.

(42) Chen, Q.; Luo, J.; He, R.; Lai, H.; Ren, S.; Jiang, Y.; Wan, Z.; Wang, W.; Hao, X.; Wang, Y.; Zhang, J.; Constantinou, I.; Wang, C.; Wu, L.; Fu, F.; Zhao, D. Unveiling Roles of Tin Fluoride Additives in High-Efficiency Low-Bandgap Mixed Tin-Lead Perovskite Solar Cells. *Adv. Energy Mater.* **2021**, *11* (29), 2101045.

(43) Zhu, H.; Liu, A.; Shim, K. I.; Jung, H.; Zou, T.; Reo, Y.; Kim, H.; Han, J. W.; Chen, Y.; Chu, H. Y.; Lim, J. H.; Kim, H. J.; Bai, S.; Noh, Y. Y. High-Performance Hysteresis-Free Perovskite Transistors through Anion Engineering. *Nat. Commun.* **2022**, *13* (1), 1741.

(44) Liao, W.; Zhao, D.; Yu, Y.; Grice, C. R.; Wang, C.; Cimaroli, A. J.; Schulz, P.; Meng, W.; Zhu, K.; Xiong, R. G.; Yan, Y. Lead-Free Inverted Planar Formamidinium Tin Triiodide Perovskite Solar Cells Achieving Power Conversion Efficiencies up to 6.22%. *Adv. Mater.* **2016**, *28* (42), 9333−9340.

(45) Taddei, M.; Smith, J. A.; Gallant, B. M.; Zhou, S.; Westbrook, R. J. E.; Shi, Y.; Wang, J.; Drysdale, J. N.; McCarthy, D. P.; Barlow, S.; Marder, S. R.; Snaith, H. J.; Ginger, D. S. Ethylenediamine Addition Improves Performance and Suppresses Phase Instabilities in Mixed-Halide Perovskites. *ACS Energy Lett.* **2022**, *7* (12), 4265−4273.

(46) Jariwala, S.; Kumar, R. E.; Eperon, G. E.; Shi, Y.; Fenning, D. P.; Ginger, D. S. Dimethylammonium Addition to Halide Perovskite Precursor Increases Vertical and Lateral Heterogeneity. *ACS Energy Lett.* **2022**, *7* (1), 204−210.

(47) Lee, S. J.; Shin, S. S.; Kim, Y. C.; Kim, D.; Ahn, T. K.; Noh, J. H.; Seo, J.; Seok, S., Il. Fabrication of Efficient Formamidinium Tin Iodide Perovskite Solar Cells through SnF2-Pyrazine Complex. *J. Am. Chem. Soc.* **2016**, *138* (12), 3974−3977.